Journal of Global Positioning Systems
Vol. 22, Issue 2:175-195
DOI:10.5081/jgps.22.2.175

ED-SA-BiConvGRU: A Deep Learning Model for Ionosphere Prediction considering RMSE during Geomagnetic Storm in Australia

Tu Yuan[1,2], ***Yize Zhang***[1], ***Hanwen Yan***[1], ***Junping Chen***[1]

[1] Shanghai Astronomical Observatory, Chinese Academy of Sciences, Shanghai 200030, China; University of Chinese Academy of Sciences, Beijing 100049, China

[2] ShanghaiTech University, Shanghai 200030, China

Corresponding author: Yize Zhang; Email: zhyize@shao.ac.cn

Abstract—Located at the core of the Equatorial Ionization Anomaly (EIA), the ionospheric Total Electron Content (TEC) in the Australian region experiences highly complex spatiotemporal evolution, which significantly degrades the accuracy of regional Global Navigation Satellite System (GNSS) positioning and navigation. Existing prediction methods—including traditional physical models and basic machine learning techniques—often overlook the intrinsic uncertainty and error dynamics of ionospheric products, failing to capture the abrupt spatiotemporal variations during severe geomagnetic storms. To address these limitations, this research develops a deep learning model named ED-SA-BiConvGRU, utilizing observation data from 70 Australian Regional GNSS Network (ARGN) stations (2021–2025). Distinct from uncertainty-aware methods that estimate predictive uncertainty from the model output, this study uses the Root Mean Square Error (RMSE) information provided with the ionospheric product as an observed product-quality indicator for TEC forecasting. Because TEC and RMSE originate from the same ionospheric product-processing chain, this strategy introduces information related to input reliability without requiring external space-weather indices or additional multisource data synchronization. The RMSE indicator is incorporated into an Encoder-Decoder architecture with Self-Attention and Bidirectional Convolutional Gated Recurrent Units, enabling the model to condition its spatiotemporal feature representation on the quality information associated with the input TEC product. Experimental results across the entire 2025 test set (comprising six major geomagnetic storms) demonstrate that the ED-SA-BiConvGRU-A (with RMSE) combination achieved an average RMSE of 1.43 TECu, representing a relative RMSE reduction of 15.4% compared with the ED-SA-BiConvGRU-B configuration without RMSE. This indicates that incorporating RMSE indices allows the model to better perceive data reliability and track ionospheric irregularities during intense storm periods. Furthermore, as the model relies exclusively on author-generated regional ionospheric maps (RIMs), it achieves high-precision forecasting without the overhead of external geophysical indices, providing a more efficient and lightweight deep learning approach for complex space weather environments.

Key Words—Geomagnetic storms, deep Learning, ED-SA-BiConvGRU, mid- to Low-Latitude

1. INTRODUCTION

The ionosphere, a layer of Earth's upper atmosphere ionized by solar radiation, exhibits a spatiotemporal distribution that directly influences electromagnetic wave propagation. Consequently, it plays a critical role in fields such as geodesy, navigation, and communications. The ionosphere in mid- to low-latitude regions, in particular, is subject

Editor-In-Charge: Dr. Ya Zhang

to complex multi-factor coupling involving solar activity, geomagnetic disturbances, and atmospheric fluctuations, leading to highly intricate and variable evolutionary characteristics [1–3]. During geomagnetic storms, the solar wind-magnetosphere interaction induces severe disturbances in ionospheric electron density. This process significantly amplifies spatiotemporal nonlinearity and frequently triggers intense ionospheric irregularities. A typical manifestation of these disturbances is the EIA (Equatorial Ionization Anomaly), characterized by the formation of dual electron density crests in the mid- to low-latitude zones of both hemispheres. Australia, situated at the core of the EIA, consequently experiences more pronounced ionospheric disturbances during geomagnetic storms compared to many other regions [4]. As GNSS satellite signals traverse the ionosphere, these complex ionospheric variations cause signal delay and refraction, thereby substantially degrading GNSS positioning and navigation accuracy.

Traditional ionospheric prediction models include empirical models and broadcast models, such as the BDGIM, Klobuchar, IRI, and NeQuick models. Krankowski et al. applied an Autoregressive Moving Average (ARMA) model to predict ionospheric TEC at different sites in Europe from 1995 to 2001. The results demonstrated that the ARMA model achieved high accuracy in short-term (a few hours) predictions, with errors around 5% of the actual TEC values [5]. However, due to the inherent nonlinearity of the ionosphere, traditional empirical or theoretical ionospheric models are limited in their capacity to accurately capture its spatiotemporal variations, which consequently constrains positioning precision during geomagnetic storms in the EIA region. Therefore, the development of a high-precision ionospheric model tailored to this region holds significant practical importance [6]. With the advancement of artificial intelligence (AI) technologies, an increasing number of researchers have turned to data-driven approaches, particularly artificial neural networks (ANNs), to enable deep learning-based ionospheric prediction. Neural networks are data-driven modeling techniques inspired by a simplified structure of the human brain, capable of parallel processing complex nonlinear processes. These networks also show great potential for predicting ionospheric variability, as they can learn patterns and regularities from specific data, thus enabling precise forecasting of ionospheric trends and changes.

Commonly used neural network models include Long Short-Term Memory (LSTM) networks and Gated Recurrent Unit (GRU). Compared to the LSTM, the GRU has a simpler structure, comprising only an update gate and a reset gate, which results in fewer parameters and higher training efficiency. The Convolutional Gated Recurrent Unit (ConvGRU) is a deep learning model that integrates a Convolutional Neural Network (CNN) with a GRU. Compared with the standard GRU, ConvGRU is capable of processing time series data while also capturing its spatial features. The core concept of ConvGRU is to replace the fully connected operations in GRU with convolutional operations, enabling the model to capture temporal dependencies and simultaneously extract spatial features—such as local spatial correlations and pattern distributions—from the input data [7]. However, while ConvGRU performs well during geomagnetic quiet periods and in low-latitude regions, its prediction error increases significantly during strong geomagnetic storms within the EIA region [8], underscoring its limitations in handling complex ionospheric characteristics. The Bidirectional LSTM (Bi-LSTM) model simultaneously considers both forward and backward temporal dependencies in the sequence, capturing more contextual information, thereby enhancing the stability and accuracy of the model [9]. Unlike traditional LSTM, Bi-LSTM improves the modeling ability of temporal data by utilizing the outputs of both forward and backward LSTM units, resulting in higher stability in ionospheric predictions for long time series. However, despite Bi-LSTM's ability to capture rich temporal dependencies, it still struggles to effectively handle complex spatial features like the Equatorial Ionization Anomaly (EIA), especially during strong geomagnetic storms, where its performance deteriorates [10]. Hybrid deep learning models, while promising for capturing complex spatiotemporal dependencies, incur high computational costs due to the need to process large volumes of data. This significantly limits their training efficiency and real-time prediction capabilities. The ED architecture addresses part of this issue by employing a downsampling strategy that progressively compresses the spatial dimensions of input data, thereby improving both training and inference efficiency, making it particularly suitable for long sequences and large-

scale datasets [11].

Uncertainty-aware deep learning has been extensively investigated in meteorology and remote sensing through probabilistic networks, Bayesian inference, ensemble learning, and other approaches. Most of these methods aim to estimate the uncertainty or confidence interval of the model output. The contribution of the present study is different from this general line of research. Rather than generating posterior predictive uncertainty, this study uses RMSE information provided by the ionospheric product as an observed product-quality indicator and introduces it directly into the TEC forecasting process. Existing deep learning models for ionospheric prediction commonly incorporate external environmental parameters as auxiliary inputs. For example, previous studies have introduced sunspot number, solar-wind velocity, and geomagnetic indices such as Dst, Kp, and ap to represent the external drivers of ionospheric variation [12–14]. These indices characterize the large-scale solar and geomagnetic environment but are obtained from data sources different from the TEC product and may require additional acquisition and temporal synchronization. In contrast, the TEC and RMSE information used in this study originate from the same ionospheric product-processing chain and share a consistent temporal reference. Therefore, RMSE can be used as a readily available quality indicator associated with the input TEC product, without introducing an additional external data source.

The unique contribution of this approach is thus not the general concept of uncertainty-aware learning, but the problem-specific use of routinely provided ionospheric product-quality information for storm-time TEC prediction. In the proposed ED-SA-BiConvGRU model, RMSE is treated as an auxiliary conditioning feature rather than as a prediction target or a posterior confidence estimate. This design allows the network to adjust its spatiotemporal representation according to changes in the quality information associated with the input TEC product. It also preserves a single-source processing pipeline, which reduces the data-acquisition and synchronization requirements of methods that rely on multiple external space-weather indices.

Accordingly, this study proposes the ED-SA-BiConvGRU model for regional ionospheric TEC prediction during geomagnetic storms. Its main contributions are threefold. First, RMSE information that is normally distributed as ionospheric product-quality information is repurposed as an auxiliary feature for TEC forecasting. Second, the RMSE indicator is integrated with an Encoder-Decoder, Self-Attention, and Bidirectional ConvGRU framework so that the spatiotemporal representation of TEC can be conditioned on information related to input-product reliability. Third, the approach is evaluated using geomagnetic-storm events in the Australian Equatorial Ionization Anomaly region, demonstrating the practical value of a single-source TEC–RMSE prediction strategy without relying on external geophysical indices. Section 2 describes the proposed model architecture, Section 3 introduces the data and preprocessing procedure, Section 4 presents the experimental results and discussion, and Section 5 summarizes the conclusions and future work.

2. ED-SA-BiConvGRU Model

The architecture proposed in this study integrates an Encoder, a Decoder, and a Self-Attention Bidirectional Convolutional Gated Recurrent Unit (SA-BiConvGRU), forming the complete ED-SA-BiConvGRU model. The Encoder extracts spatial features from the input data through multiple convolutional layers and captures temporal dependencies using BiConvGRU units. The SA module enhances the model's capacity to capture long-range spatiotemporal correlations by computing attention weights between hidden states. Finally, the Decoder employs deconvolutional (transposed convolutional) layers to restore the spatial dimensions and progressively reconstructs future TEC.

Fig. 1 illustrates the overall architecture of the proposed ED-SA-BiConvGRU model, in which the “Input Module” at the bottom of the figure performs the fusion of multi-source input data, which comprises past Vertical Total Electron Content (VTEC) products alongside ionospheric Root Mean Square Error (RMSE) indices. The orange solid box in the middle delineates the hierarchical Encoder [11], constructed from forward and backward ConvGRU layers, each of which extracts high-dimensional spatiotemporal features through convolutional operations. Encapsulated within the blue dashed box is the computational detail of the core SA module, which captures global dependencies among the input features using the Query-Key-Value (Q-K-V) mechanism [2]. Finally, the blue solid box at the top represents the Decoder, which employs transposed

convolutional (ConvTranspose2d) layers to progressively restore the spatial resolution of the feature maps, effectively reconstructing the abstract representations compressed by the Encoder. Through the Output Module, the model ultimately generates a predicted ionospheric VTEC distribution map, which matches the spatial resolution of the input.

1.1 Overall framework and quality-information fusion

The proposed ED-SA-BiConvGRU model consists of a convolutional feature encoder, four stacked bidirectional self-attention ConvGRU layers, four unidirectional self-attention ConvGRU decoder layers, and a convolutional output head. As illustrated in Fig. 1, the model receives a sequence of historical VTEC maps together with the corresponding RMSE quality indicators and predicts the VTEC map at the next epoch. The bidirectional structure is applied only to the observed historical window and does not access any future VTEC observations.

Let $X_t \in \mathbb{R}^{1\times H\times W}$ denote the VTEC map at epoch t, where H=11 and W=9, and let r_t denote its associated RMSE quality indicator. The VTEC map is first transformed into a 64-channel spatial representation through one 1×1 convolution and two 3×3 convolutions:

$$F_t = f_{enc}(X_t) \quad (1)$$

where $F_t \in \mathbb{R}^{64\times H\times W}$. The RMSE indicator is expanded to the same spatial dimensions and concatenated with the encoded VTEC feature:

$$U_t = [F_t; \mathcal{B}(r_t)] \quad (2)$$

where $\mathcal{B}(\cdot)$ denotes spatial broadcasting and $[\cdot\,;\cdot]$ denotes channel-wise concatenation. Unlike external geomagnetic indices, RMSE is treated as quality information associated with the ionospheric product itself. Introducing it before recurrent encoding allows the subsequent gates and attention operations to condition their feature extraction on changes in the reliability of the input product.

1.2 Bidirectional self-attention ConvGRU encoder

ConvGRU replaces the fully connected transformations of a conventional GRU with convolutional operations, thereby preserving the spatial organization of the regional VTEC maps. For an input feature U_t and the previous hidden state H_{t-1}, the convolutional output is divided into reset, update, and candidate components:

$$\begin{cases} [R_t, Z_t, G_t] = \mathrm{GN}\,(W_c * [U_t;\, H_{t-1}] + b_c) \\ r_t^g = \sigma(R_t),\;\; z_t = \sigma(Z_t) \\ \widetilde{H_t} = \tanh(r_t^g \odot H_{t-1} + G_t) \\ H_t' = (1 - z_t) \odot H_{t-1} + z_t \odot \widetilde{H_t} \end{cases} \quad (3)$$

where * denotes convolution, $\odot$ denotes element-wise multiplication, σ is the sigmoid function, and GN denotes group normalization. The reset gate determines how much previous information contributes to the candidate state, whereas the update gate controls the balance between the previous state and the newly extracted spatiotemporal information.

To capture temporal dependencies in both directions within the historical input window, the encoder processes the sequence using forward and backward SA-ConvGRU cells:

$$\begin{cases} \vec{H}_t^{(l)} = \mathcal{F}^{(l)}(U_t^{(l)}, \vec{H}_{t-1}^{(l)}) \\ \overleftarrow{H}_t^{(l)} = \mathcal{B}^{(l)}(U_t^{(l)}, \overleftarrow{H}_{t+1}^{(l)}) \\ H_t^{(l)} = \left[\vec{H}_t^{(l)}; \overleftarrow{H}_t^{(l)}\right],\;\; \mathrm{l} = 1, \ldots, 4 \end{cases} \quad (4)$$

The forward branch describes the chronological development of the ionosphere, while the backward branch extracts complementary contextual information from the same observed sequence. Their outputs are concatenated along the channel dimension and passed to the next encoder layer. Because both branches operate exclusively on the preceding 48 observed epochs, the bidirectional operation does not introduce future target information.

1.3 Spatial self-attention memory mechanism

Although convolutional recurrence is effective in modeling local spatial relationships, its receptive field may be insufficient for representing long-range dependencies between geographically separated regions. This limitation is particularly important during geomagnetic storms, when the Equatorial Ionization Anomaly and associated high-gradient structures can extend across a large part of the Australian region. Therefore, a spatial self-attention memory module is embedded in each SA-ConvGRU cell.

The intermediate hidden state H_t' and the previous memory state M_{t-1} are projected using 1×1 convolutions:

$$\begin{cases} Q_t = W_q * H_t',\;\; K_t^h = W_k * H_t',\;\; = W_v * H_t' \\ K_t^m = W_{km} * M_{t-1},\quad V_t^m = W_{vm} * M_{t-1} \end{cases} \quad (5)$$

After flattening the spatial dimensions into $P=H\times W$ positions, two attention matrices are calculated:

$$A_t^h = \text{softmax}\left(Q_t K_t^h\right), A_t^m = \text{softmax}\left(Q_t K_t^m\right) \quad (6)$$

The corresponding spatially aggregated features are

$$Z_t^h = A_t^h V_t^h,\ Z_t^m = A_t^m V_t^m \quad (7)$$

The attended hidden and memory features are concatenated and transformed to update the memory state:

$$\begin{cases} Z_t = W_z * [Z_t^h;\ Z_t^m] \\ [O_t, \bar{G}_t, I_t] = W_m * [Z_t; H_t'] \\ i_t = \sigma(I_t) \\ M_t = (1 - i_t) \odot M_{t-1} + i_t \odot \tanh(\bar{G}_t) \\ H_t = \sigma(O_t) \odot M_t \end{cases} \quad (8)$$

This mechanism enables the network to adaptively relate every grid point to all other grid points and to preserve information from previous epochs through the memory state. Consequently, the model can represent both local VTEC gradients and large-scale spatial coupling during geomagnetic disturbances.

1.4 Decoder and VTEC prediction

The decoder contains four stacked unidirectional SA-ConvGRU layers. Their initial hidden and memory states are obtained from the corresponding encoder layers, allowing the spatiotemporal information extracted from the historical sequence to be transferred to the prediction stage. Unlike the bidirectional encoder, the decoder evolves only in the forward temporal direction.

Because the convolutional feature encoder preserves the 11×9 spatial resolution, no spatial upsampling is required. The output of the final decoder layer is transformed by two 3×3 convolutional layers and one 1×1 convolution:

$$\hat{X}_{T+1} = f_{out}(D_{T+1}) \quad (9)$$

where D_{T+1} is the output of the final decoder layer and $\hat{X}_{T+1}$ is the predicted VTEC map. The model is optimized using the mean squared error:

$$\mathcal{L}_{MSE} = \frac{1}{NHW} \sum_{n=1}^{N} \sum_{i=1}^{H} \sum_{j=1}^{W} (\hat{X}_{n,i,j} - X_{n,i,j})^2 \quad (10)$$

The theoretical contribution of the proposed framework lies in the coordinated use of three complementary mechanisms. The bidirectional ConvGRU extracts temporal context from the complete observed window, the spatial self-attention memory module models nonlocal ionospheric relationships, and the RMSE quality indicator conditions the recurrent representation on the reliability information associated with the input product. Their integration enables the model to represent rapid temporal evolution, large-scale spatial coupling, and changes in product quality within a unified storm-time VTEC prediction framework.

3. DATA PREPROCESSING

Australia is located near the southern crest of the Equatorial Ionization Anomaly, where ionospheric VTEC exhibits complex spatiotemporal variations, particularly during geomagnetic storms. The ionospheric products used in this study were not obtained from an IGS analysis center. Instead, regional ionospheric maps were generated by the authors using dual-frequency GNSS observations collected at 70 Australian Regional GNSS Network (ARGN) stations distributed over the region 12.5°S-37.5°S and 115°E-155°E. The station distribution is shown in Fig. 2. At each 30-min epoch, the station observations were used to estimate regional VTEC through a spherical harmonic model. The resulting VTEC estimates and their associated RMSE information were mapped onto a 2.5°latitude by 5°longitude grid, producing regional maps with 11×9 grid points. To avoid confusion with the global ionospheric maps distributed by IGS analysis centers, these author-generated products are hereafter referred to as regional ionospheric maps (RIMs).

To construct the dataset, this study selected 30 strong geomagnetic-storm events from 2021 to 2025. The specific periods and minimum Dst values of these events are listed in Table Ⅰ. For each event, the main and recovery phases were defined relative to the occurrence time of the minimum disturbance storm time (Dst) index. The event interval covers the preceding 72 h and the subsequent 72 h, which is sufficient to characterize the main and recovery phases of the storm. According to the Dst-based intensity classification, an event was classified as a strong geomagnetic storm when its minimum Dst value was below -80 nT [10].

Before constructing the sliding-window samples, the 30 geomagnetic-storm events were arranged chronologically and partitioned at the event level into training, validation, and test sets at a ratio of 7:1:2. Specifically, the first 21 events, extending from 2021 through the event at DOY

214–220 in 2024, were used for training; the subsequent three events at DOY 222–228, 253–259, and 311–317 in 2024 were used for validation; and the final six events in 2025 were retained as an independent test set. Thus, the three subsets consist of chronologically ordered but distinct geomagnetic-storm events, and no event is shared among them. Each event contains 288 epochs at a temporal resolution of 30 min. Sliding-window samples were generated independently within each event using the preceding 48 epochs (24 h) to predict the next epoch, with a stride of one. This procedure yielded 5,040 training samples, 720 validation samples, and 1,440 test samples. No sliding window was allowed to cross an event or dataset boundary, and only the training samples were shuffled during mini-batch loading. The normalization parameters for TEC and RMSE were calculated exclusively from the training set and then applied unchanged to the validation and test sets, thereby preventing information leakage among the three subsets.

The spherical harmonic (SH) method is employed to model regional VTEC products from the 70 GNSS stations. VTEC maps are generated for the Australian region on a spatial grid with a resolution of 2.5° in latitude and 5° in longitude, resulting in a grid of 11 × 9 points. The corresponding spherical harmonic expansion is expressed as follows [15]:

$$VTEC(\theta,\phi,t) = \sum_{n=0}^{N}\sum_{m=0}^{n}[A_n^m(t)\cos(m\phi) + B_n^m(t)\sin(m\phi)]P_n^m(\cos\theta) \quad (11)$$

In the equation above, θ represents the geographic colatitude, φ is the geographic longitude, A_n^m and B_n^m denotes the unknown spherical harmonic coefficients, N is the highest order, $(N+1)^2$ represents the total number of coefficients, P_n^m is the orthonormalized Legendre function, m is the order that determines the latitude resolution, and n is the degree that governs the periodic variation in the longitudinal direction.

The regional VTEC and its associated RMSE were obtained from the same weighted least-squares spherical harmonic adjustment. At epoch t, the observation equation can be written as:

$$y_t = A_t a_t + \mathcal{E}_t \quad (12)$$

where y_t contains the VTEC observations at the ionospheric pierce points, A_t is the spherical harmonic design matrix, and a_t contains the unknown spherical harmonic coefficients. The coefficient estimates are obtained by:

$$\hat{a}_t = (A_t^T P_t A_t)^{-1} A_t^T P_t y_t \quad (13)$$

where P_t is the observation-weight matrix. Let

$$v_t = y_t - A_t \hat{a}_t \quad (14)$$

denote the fitting residuals. The posterior variance factor is calculated as

$$\hat{\sigma}_{0,t}^2 = \frac{v_t^T P_t v_t}{n_t - u} \quad (15)$$

where n_t is the number of observations and u is the number of estimated coefficients. The covariance matrix of the estimated coefficients is:

$$C_{\hat{a},t} = \hat{\sigma}_{0,t}^2 (A_t^T P_t A_t)^{-1} \quad (16)$$

For grid point g, let b_g denote the spherical harmonic basis vector. The gridded VTEC and its formal RMSE are then calculated as:

$$VTEC_{g,t} = b_g^T \hat{a}_t,$$
$$\mathrm{RMS}E_{g,t} = \sqrt{b_g^T C_{\hat{a},t} b_g} \quad (17)$$

Therefore, RMSE represents the formal uncertainty of the spherical-harmonic VTEC estimate at each grid point. It reflects not only the magnitude of the fitting residuals but also the observation weights and the spatial geometry represented by the design matrix.

Because VTEC and RMSE are generated from the same spherical harmonic adjustment, they are not statistically independent, and some degree of correlation is expected. Nevertheless, this relationship does not constitute an algebraic circularity. The gridded VTEC is determined by the estimated spherical harmonic coefficients, whereas RMSE is determined by the residual variance and the propagated coefficient covariance. Consequently, two epochs with similar VTEC magnitudes may have different RMSE values because of differences in observation coverage, residual dispersion, weighting, or estimation geometry. In the proposed model, RMSE is therefore interpreted as a product-quality conditioning variable rather than as an independent physical driver. Only historical RMSE values available within the input window are used; no RMSE information from the target epoch is included. This prevents the target VTEC from being

indirectly introduced through its contemporaneous fitting uncertainty.

4. EXPERIMENTS AND DISCUSSION

To comprehensively evaluate prediction accuracy, agreement, stability, and tail-error behaviour, this study employs five complementary metrics: the root mean square error (RMSE), mean absolute error (MAE), Pearson correlation coefficient (CC), residual standard deviation (Residual SD), and the 95th-percentile absolute error (P95AE). RMSE assigns greater weight to relatively large prediction deviations, whereas MAE represents the average magnitude of the absolute prediction errors and is less sensitive to extreme values. CC measures the correlation and trend consistency between the predicted and ground-truth values. Residual SD measures the dispersion of the signed prediction residuals, whereas P95AE denotes the value below which 95% of the absolute prediction errors fall. Therefore, lower RMSE, MAE, Residual SD, and P95AE values together with a higher CC value indicate better prediction performance. Their respective calculation formulas are as follows:

$$\begin{cases} RMSE = \sqrt{\dfrac{1}{N}\sum_{i=1}^{N}(TEC_{prediction}^{i} - TEC_{\text{observation}}^{i})^2} \\ MAE = \dfrac{1}{N}\sum_{i=1}^{N}\left|TEC_{prediction}^{i} - TEC_{\text{observation}}^{i}\right| \\ CC = \dfrac{cov\left(TEC_{prediction}, TEC_{\text{observation}}\right)}{\sigma_{TEC_{prediction}} \cdot \sigma_{TEC_{\text{observation}}}} \end{cases} \tag{18}$$

In the equation above, $TEC_{prediction}^{i}$ represents the predicted TEC value of the (i)-th sample, $TEC_{\text{observation}}^{i}$ represents the observed TEC value of the (i)-th sample, (N) is the total number of samples, cov denotes the covariance, and σ represents the standard deviation.

The ED-SA-BiConvGRU model was implemented using PyTorch. The input and output VTEC maps have a spatial dimension of 11 × 9 grid points. For each sample, the preceding 48 epochs, corresponding to 24 h at the 30-min temporal resolution, were used to predict the next epoch. The model consists of four stacked recurrent layers, with both the hidden-state dimension and attention dimension set to 64. The convolutional kernel size was set to 3 × 3, and the batch size was set to 8. The model was trained using the Adam optimizer with an initial learning rate of 1×10^{-4} and the mean squared error as the loss function. The maximum number of training epochs was 40, and early stopping with a patience of 8 epochs was applied according to the validation loss. The teacher-forcing rate was set to 0.5 during training and to zero during validation and testing. The model checkpoint with the lowest validation loss was retained for final evaluation. For clarity and reproducibility, the complete architecture and training configuration of the ED-SA-BiConvGRU model is summarized in Table II.

For the controlled comparison between ED-SA-BiConvGRU-A and ED-SA-BiConvGRU-B, all architecture and training settings were kept identical, with the RMSE input being the only difference. The GRU and ConvGRU baselines were evaluated using the same data partition and evaluation protocol while retaining their respective architecture-specific configurations. The input length of 48 epochs was adopted because it covers a complete 24-h ionospheric variation cycle and provides sufficient temporal context for short-term prediction. The hidden-state dimension of 64 and the four-layer recurrent structure were used to balance spatiotemporal representation capacity, training stability, and computational complexity. Similarly, the 3 × 3 convolutional kernel captures local spatial correlations without introducing excessive parameters. Since the primary objective of this study is to investigate the contribution of RMSE as an auxiliary input under controlled experimental conditions, a systematic parameter sensitivity analysis is beyond the present scope and will be considered in future work.

A: Prediction during the main phase of geomagnetic storms

To evaluate the impact of the ionospheric Root Mean Square Error (RMSE) on prediction

performance, this study explores two different combinations of input parameters: ED-SA-BiConvGRU-A (with RMSE) and ED-SA-BiConvGRU-B (without RMSE). We selected the most severe geomagnetic storm event in the test set (2025 DOY 103-109) for result analysis. As shown in Fig. 3, both panels (a) and (b) depict the main phase of the geomagnetic storm. The results reveal that ionospheric anomalies occur more frequently in the mid- to low-latitude regions at UT 06:00, and the prediction errors of all models are predominantly concentrated in high-gradient regions where VTEC transitions from high (red) to low (blue) values. We further calculated the prediction residuals between the ED-SA-BiConvGRU-A and ED-SA-BiConvGRU-B combinations and the ground truth, as shown in Fig. 4. It is found that for the ED-SA-BiConvGRU-A combination, over 80% of the absolute residuals are within 2 TECu, and more than 60% are controlled within 1 TECu. In contrast to the ED-SA-BiConvGRU-B combination, which exhibits significant underestimation in regions with intense TEC gradients, the A combination—by leveraging the RMSE index as a dynamic weight indicator—demonstrates a much stronger capability in tracking rapid fluctuations and mitigating large-scale biases during the storm's peak.

Table III compares the proposed ED-SA-BiConvGRU configurations with two representative baseline models, GRU and ConvGRU, over the six geomagnetic storm events in the 2025 test set, with the best performance highlighted in bold. GRU provides a temporal prediction baseline without explicitly modelling spatial correlations, whereas ConvGRU incorporates convolutional operations to capture local spatiotemporal dependencies. The inclusion of these two baselines enables the proposed method to be evaluated against both temporal-only and spatiotemporal recurrent models. In addition, ED-SA-BiConvGRU-A and ED-SA-BiConvGRU-B use the same network architecture, training settings, and data partition, with the ionospheric RMSE input being the only difference. Therefore, their comparison constitutes a controlled ablation study that specifically evaluates the contribution of RMSE. ED-SA-BiConvGRU-A achieves the best overall performance among the evaluated models, with an RMSE of 1.43 TECu, an MAE of 0.96 TECu, and a CC of 0.985. Compared with ED-SA-BiConvGRU-B, its RMSE is reduced by approximately 15.4%. Its Residual SD and P95AE are also reduced from 1.63 TECu and 3.32 TECu to 1.42 TECu and 2.88 TECu, respectively. These results demonstrate that the proposed spatiotemporal architecture provides advantages over the conventional recurrent baselines and that incorporating ionospheric RMSE further improves prediction accuracy, error stability, and tail-error control under severe geomagnetic-storm conditions.

Beyond the overall numerical improvement, Figs. 3 and 4 reveal several distinct spatiotemporal characteristics. During the main phase, a pronounced VTEC enhancement develops over northern Australia at approximately 06:00 UT, producing a strong north–south gradient between the low-latitude enhancement region and southern Australia. The prediction errors are therefore spatially structured rather than randomly distributed and are mainly concentrated near the northern and northeastern high-gradient regions. ED-SA-BiConvGRU-B tends to produce broader and more coherent residual structures in these regions, indicating that it does not fully reproduce the position and amplitude of the rapidly evolving VTEC enhancement. In comparison, ED-SA-BiConvGRU-A generally produces residuals closer to zero and better preserves the location and shape of the enhanced VTEC region. This phenomenon suggests that RMSE provides useful information about regions with rapidly changing interpolation uncertainty, allowing the model to adjust its representation of sharp spatial gradients. Nevertheless, localized residuals remain near the boundaries of the enhanced region, indicating that the displacement of strong ionospheric gradients remains a major source of prediction uncertainty.

B: Prediction during the recovery phase of geomagnetic storms

During the recovery phase of the geomagnetic storm, the behavior of the low-latitude ionosphere is governed by complex physical mechanisms. As illustrated in the first and fourth columns of Fig. 5, the ionospheric TEC values gradually decline during this phase, reflecting its dissipative behavior—a process likely driven by changes in thermospheric composition and the weakening of electric field disturbances. The comparison results in Table Ⅲ and Fig. 5 further demonstrate that, compared to the ED-SA-BiConvGRU-B combination, the ED-SA-BiConvGRU-A combination demonstrates a superior ability to track the slow-varying dissipative trends of the ionosphere, particularly in characterizing the gradual weakening of the EIA peaks. While Fig. 6 shows that the B combination often produces

persistent residuals during the electron density decline, the A combination effectively captures the subtle spatiotemporal evolution of the interpolated TEC values. This suggests that the incorporation of RMSE not only helps in high-gradient detection during the main phase but also provides essential contextual information regarding ionospheric state reliability during the recovery phase, leading to higher overall prediction consistency.

During the recovery phase, the spatial evolution differs from the rapid enhancement observed during the main phase. As shown in Figs. 5 and 6, enhanced VTEC is still present over northern Australia at 00:00 and 06:00 UT, but its magnitude and spatial extent gradually decrease at 12:00 and 18:00 UT. The residuals exhibit coherent latitudinal patterns, indicating that the dominant error is associated with the timing and spatial displacement of the decaying ionospheric enhancement rather than with spatially uniform bias. ED-SA-BiConvGRU-B retains relatively broad positive or negative residual regions, particularly near the northern and eastern boundaries, whereas ED-SA-BiConvGRU-A more closely follows the gradual weakening and redistribution of VTEC. This behavior indicates that RMSE is useful not only during the rapid enhancement of the main phase but also during the slower relaxation of the ionosphere, because it provides additional information on the spatial reliability of the evolving VTEC field.

5.CONCLUSION

To address the significant spatiotemporal variability of the mid- to low-latitude ionosphere under extreme conditions such as geomagnetic storms and the associated limitations in prediction accuracy, this study proposes a spatiotemporal sequence prediction framework named ED-SA-BiConvGRU, which specifically incorporates the ionospheric Root Mean Square Error (RMSE) as a key predictive feature. The model was systematically evaluated using geomagnetic storm data from the Australian ionosphere between 2021 and 2025. The experimental results demonstrate that, across all evaluation metrics, ED-SA-BiConvGRU-A with RMSE outperforms ED-SA-BiConvGRU-B without RMSE. The integration of ionospheric Root Mean Square Error (RMSE) serves as a critical quality fingerprint of the input data, enabling the model to dynamically perceive spatial uncertainties and prioritize high-gradient regions during intense storm periods. By exploiting these internal error characteristics—rather than relying on external environmental parameters—the model effectively mitigates systematic biases and enhances adaptive robustness in complex space weather environments. Furthermore, since the proposed model relies exclusively on author-generated regional ionospheric maps (RIMs) as the singular data source, it eliminates the necessity for external geophysical indices (e.g., Dst, Kp, or F10.7), which are often subject to acquisition delays or synchronization challenges. This all-in-one data approach significantly reduces the complexity of data pre-processing and simplifies the model's pipeline, facilitating a more lightweight architecture with higher computational efficiency. Consequently, this study offers a novel perspective for real-time ionospheric monitoring and high-precision forecasting without the overhead of multi-source data integration. Our future work will focus on further optimizing the model architecture, identifying auxiliary parameters more suitable for regional ionospheric prediction, and developing more efficient and adaptive forecasting models.

Acknowledgment

The authors gratefully acknowledge ARGN for supplying the GNSS observation data used in this study.

REFERENCES

1. Hafteh V. M., Mahmoudian A., Yoshikawa A. (2024), Mid□latitude Study of Ionospheric Variation over Iran Associated with Equatorial Ionization Anomaly (EIA), and Artificial Neural Networks Model Development, Space Weather, Vol. 22, No. 11, pp. e2024SW004032.

2. Yan X., Cai H., Xu C. (2023), A High□Precision and Lightweight Prediction Model for Global Total Electron Content, Remote Sensing, Vol. 15, No. 17, pp. 4185.

3. Yiran L., Jian W., Cheng Y. (2022), A Machine Learning□Based Method for Modeling TEC Regional Temporal□Spatial Map, Remote Sensing, Vol. 14, No. 21, pp. 5579.

4. Xiong P., Zhai D., Long C. (2021), Long Short□Term Memory Neural Network for

Ionospheric Total Electron Content Forecasting over China, Space Weather, Vol. 19, No. 4, pp. e2020SW002706.
5. Yasyukevich Y., Vasilyev R., Ratovsky K. (2020), Small□Scale Ionospheric Irregularities of Auroral Origin at Mid□latitudes during the 22 June 2015 Magnetic Storm and Their Effect on GPS Positioning, Remote Sensing, Vol. 12, No. 10, pp. 1579.
6. Bilitza D., Altadill D., Truhlik V. (2017), International Reference Ionosphere 2016: From ionospheric climate to real□time weather predictions, Space Weather, Vol. 15, No. 2, pp. 418–429.
7. Tang J., Zhong Z., Ding M. (2024), Forecast of ionospheric TEC maps using ConvGRU deep learning over China, IEEE Journal of Selected Topics in Applied Earth Observations and Remote Sensing, Vol. 17, pp. 3334–3344.
8. Jinpei C., Nan Z., Haofan L. (2022), Global forecasting of ionospheric vertical total electron contents via ConvLSTM with spectrum analysis, GPS Solutions, Vol. 26, No. 3.
9. Liu H., Wang H., Le H. (2025), CGAOA□STRA□BiConvLSTM: An automated deep learning framework for global TEC map prediction, GPS Solutions, Vol. 29, No. 1, pp. 55.
10. Li W., Zhu H., Yang F. (2025), Storm□time ionospheric model over Yunnan□Sichuan area of China based on the SSA□ConvLSTM□BiLSTM algorithm, GPS Solutions, Vol. 29, pp. 77.
11. Li L., Liu H., Le H. (2024), ED□AttConvLSTM: An Ionospheric TEC Map Prediction Model Using Adaptive Weighted Spatiotemporal Features, Space Weather, Vol. 22, No. 3.
12. Gao X., Yao Y. (2023), A storm□time ionospheric TEC model with multichannel features by the spatiotemporal ConvLSTM network, Journal of Geodesy, Vol. 97, No. 1, pp. 9.
13. Ren X., Zhao B., Ren Z. (2024), Deep learning‐based prediction of global ionospheric TEC during storm periods: Mixed CNN‐BiLSTM method, Space Weather, Vol. 22, No. 7, pp. e2024SW003877.
14. Liu R., Jiang Y. (2024), Ionospheric VTEC maps forecasting based on graph neural network with transformers, IEEE Journal of Selected Topics in Applied Earth Observations and Remote Sensing, Vol. 18, pp. 1802–1816.
15. Wang C., Xin S., Liu X. (2018), Prediction of global ionospheric VTEC maps using an adaptive autoregressive model, Earth, Planets and Space, Vol. 70, No. 1, pp. 18.

FIGURE CAPTIONS

Fig. 1. The structure and algorithm flow of the ED-SA-BiConvGRU model.
Fig. 2. Australian monitoring station distribution.
Fig. 3. Comparison of spatiotemporal prediction results for different combinations during the main phase of the 2025 geomagnetic storm on DOY 105 and DOY 106 (from left to right: Ground Truth, ED-SA-BiConvGRU-A, ED-SA-BiConvGRU-B).
Fig. 4. Prediction residual of different combinations during the main phase of the 2025 geomagnetic storm (DOY 105 and DOY 106).
Fig. 5. Comparison of spatiotemporal prediction results for different combinations during the recovery phase of the 2025 geomagnetic storm (DOY107 and DOY108).
Fig. 6. Prediction residual of different combinations during the recovery phase of the 2025 geomagnetic storm (DOY 107 and DOY 108).

TABLE CAPTIONS

Table I. Sample event division and minimum Dst values.
Table Ⅱ. Main model and training parameters of the ED-SA-BiConvGRU model.
Table Ⅲ. Performance comparison of the proposed ED-SA-BiConvGRU configurations and baseline models over the six geomagnetic storm events in the 2025 test set.

TABLES

Table Ⅰ. Sample event division and minimum Dst values.

Year	DOYs	Dst Min (nT)	Partition
2021	236-242	-82	
	305-311	-105	
2022	11-17	-91	
	69-75	-85	
	101-107	-81	
	185-191	-81	
	308-314	-92	
2023	55-61	-132	
	80-86	-163	
	111-117	-213	Train set
	252-258	-82	
	259-265	-85	
	291-297	-88	
	306-312	-163	
	332-338	-108	
2024	60-66	-112	
	81-87	-128	
	120-126	-89	
	135-141	-88	
	177-183	-107	
	214-220	-100	
	222-228	-188	Validation set
	253-259	-121	
	311-317	-101	
2025	103-109	-138	Test set
	149-155	-119	
	161-167	-101	
	218-224	-85	
	270-276	-106	
	307-313	-129	

Table Ⅱ. Main model and training parameters of the ED-SA-BiConvGRU model.

Parameter	Configuration
Input/output grid size	11×9
Input/prediction length	48 input epochs (24 h) / 1 output epoch (30 min)
Hidden/attention dimension	64/64
ConvGRU kernel	3×3, padding = 1
Loss function	Mean squared error (MSE)
Initial learning rate	1×10^{-4}
Batch size	8
Training epochs	Maximum 40 epochs; early-stopping patience = 8
Teacher-forcing rate	0.5 during training; 0 during validation and testing

Table Ⅲ. Performance comparison of the proposed ED-SA-BiConvGRU configurations and baseline models over the six geomagnetic storm events in the 2025 test set.

Model	Evaluation index (TECu)				
	RMSE	MAE	CC	Residual SD	P95AE
ED-SA-BiConvGRU-A	**1.43**	**0.96**	**0.985**	**1.42**	**2.88**
ED-SA-BiConvGRU-B	1.69	1.21	0.976	1.63	3.32
ConvGRU	1.83	1.23	0.974	1.82	3.98
GRU	1.91	1.39	0.973	1.89	4.12

FIGURES

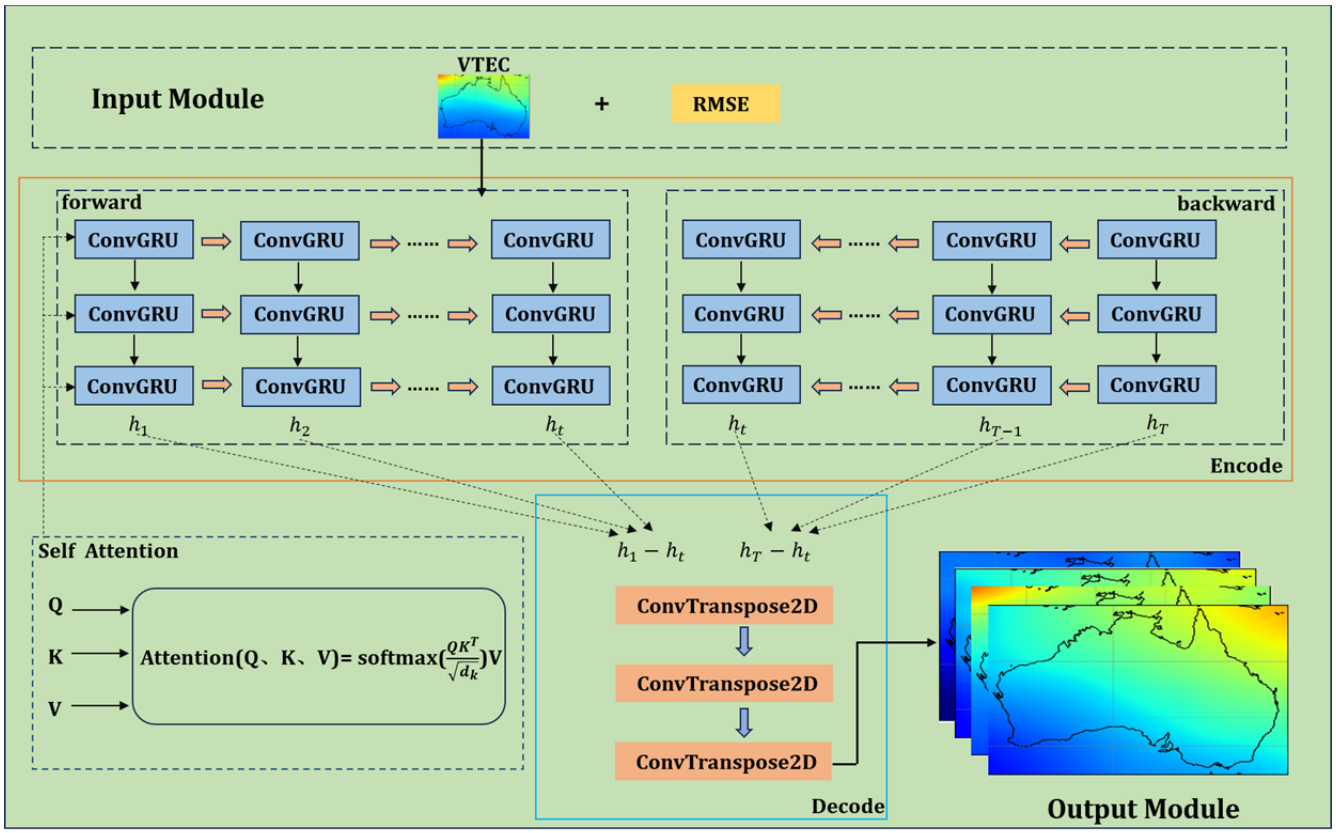


Fig. 1. The structure and algorithm flow of the ED-SA-BiConvGRU model.

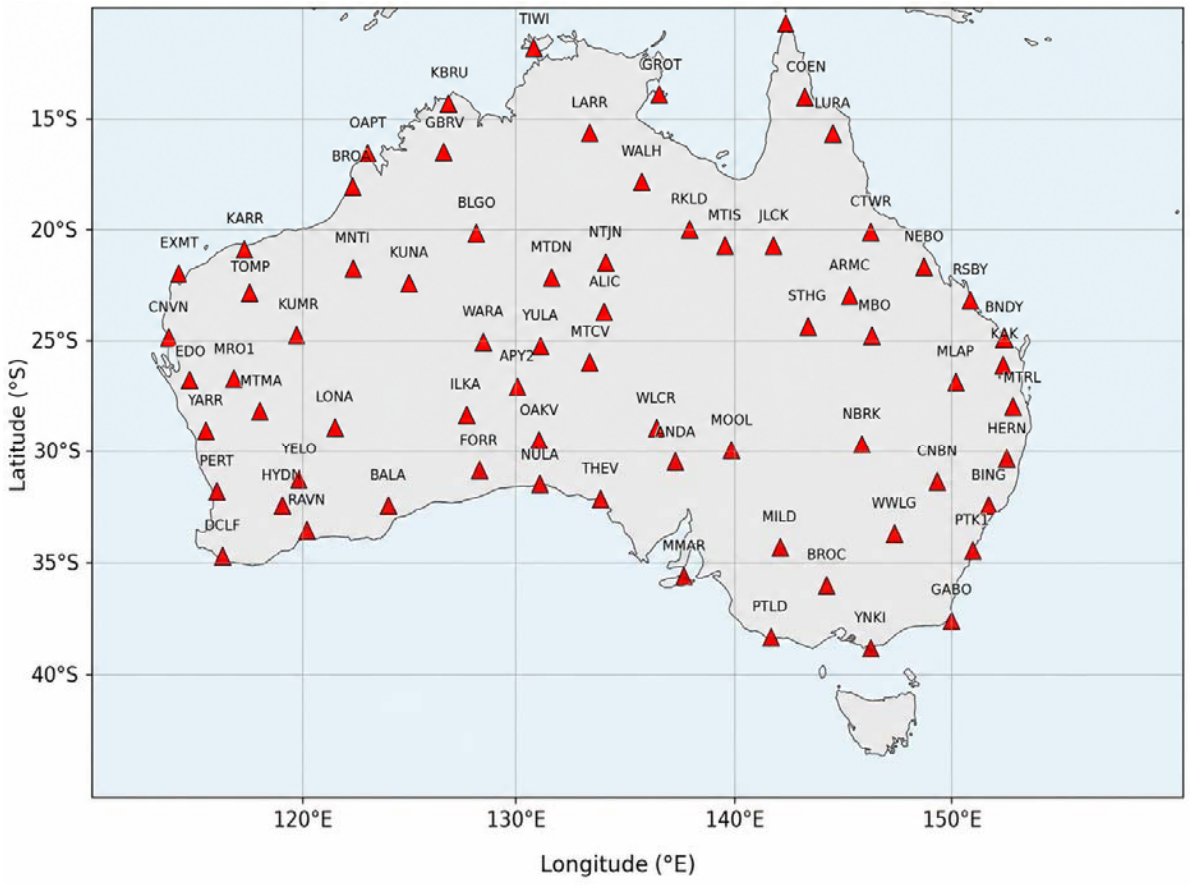
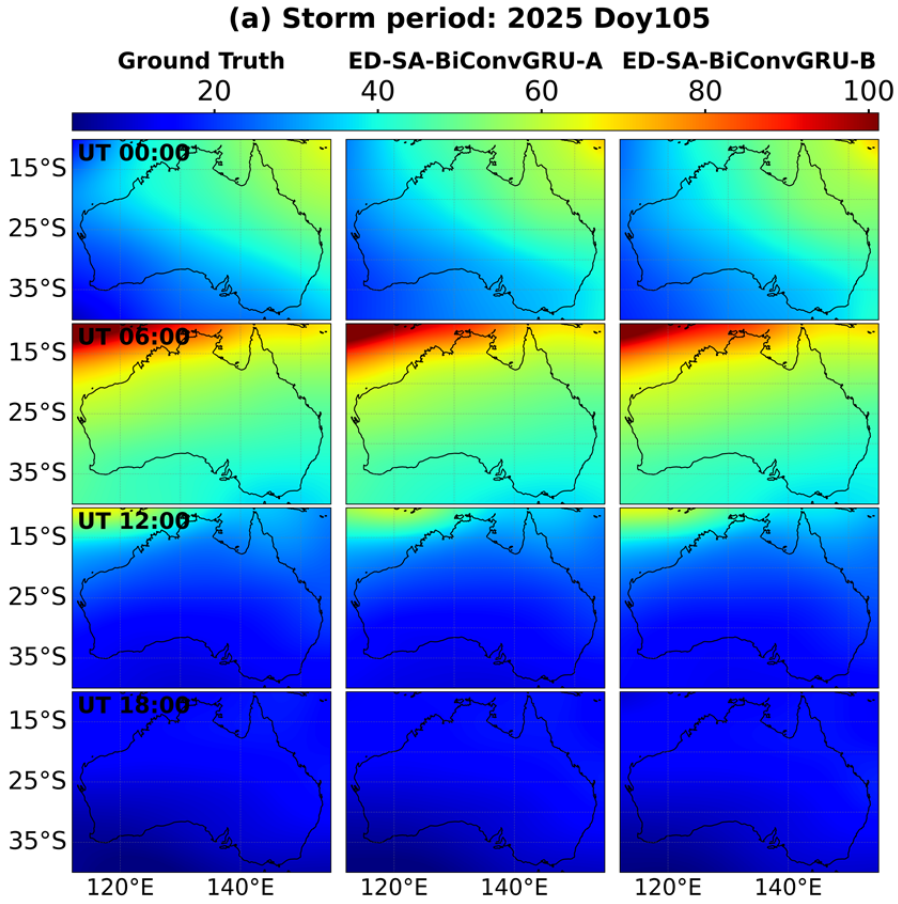


Fig. 2. Australian monitoring station distribution.


(a) Storm period: 2025 Doy105
Ground Truth
ED-SA-BiConvGRU-A
ED-SA-BiConvGRU-B
20
40
60
80
100
UT 00:00
UT 06:00
UT 12:00
UT 18:00
15°S
25°S
35°S
120°E
140°E

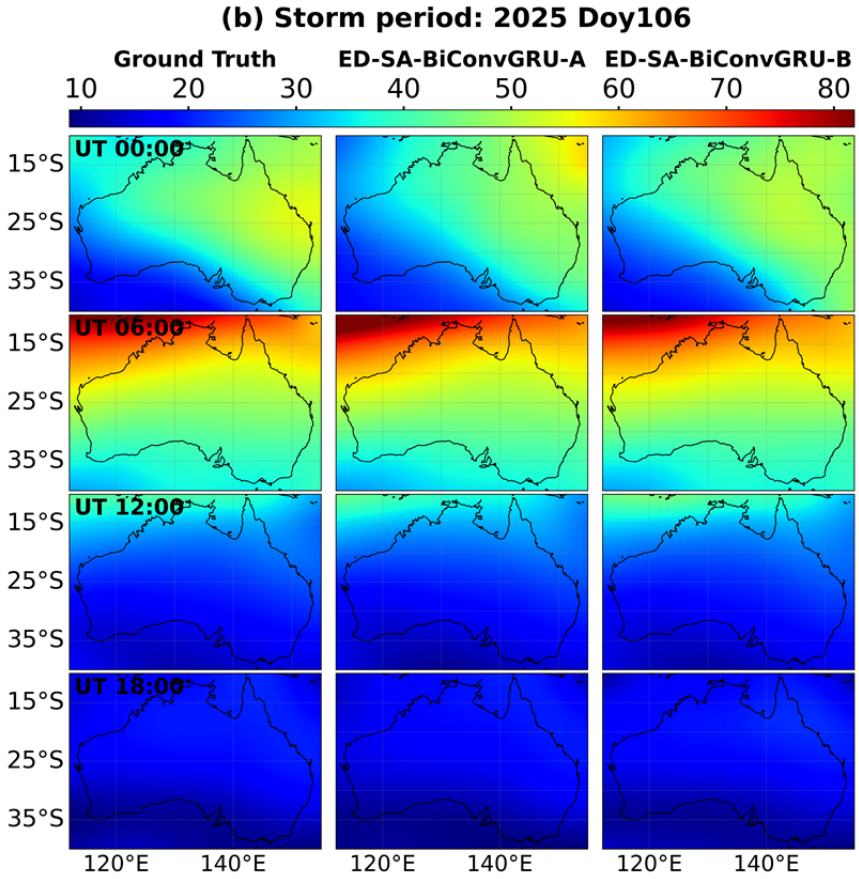
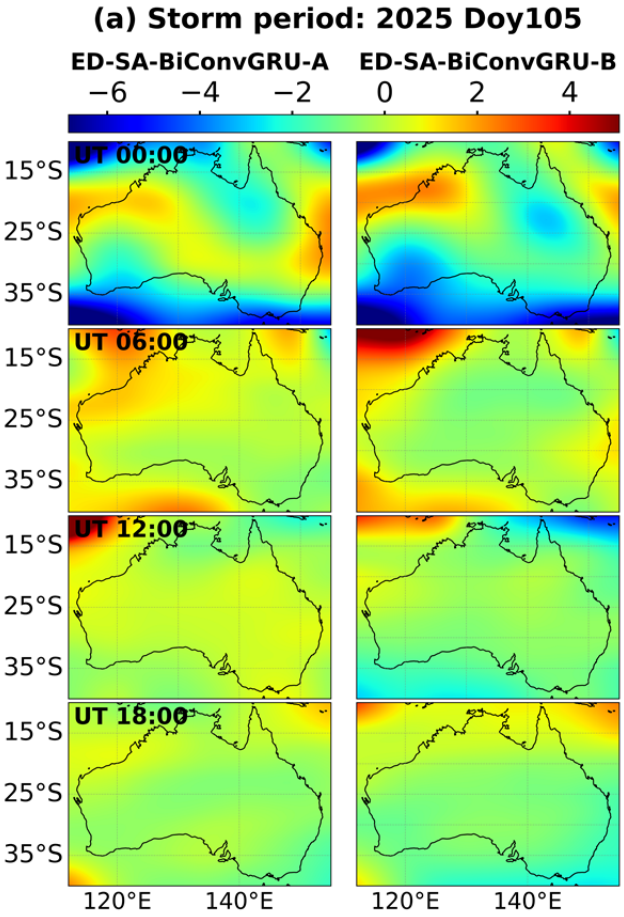


Fig. 3. Comparison of spatiotemporal prediction results (TECu) for different combinations during the main phase of the 2025 geomagnetic storm on DOY 105 and DOY 106 (from left to right: Ground Truth, ED-SA-BiConvGRU-A, ED-SA-BiConvGRU-B).


(a) Storm period: 2025 Doy105
ED-SA-BiConvGRU-A
ED-SA-BiConvGRU-B
−6
−4
−2
0
2
4
UT 00:00
UT 06:00
UT 12:00
UT 18:00
15°S
25°S
35°S
120°E
140°E

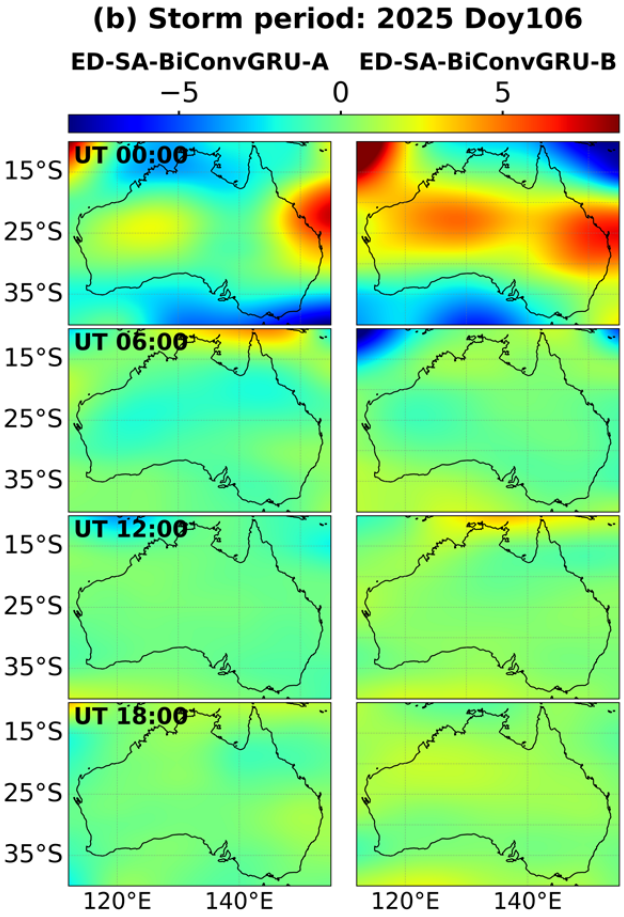
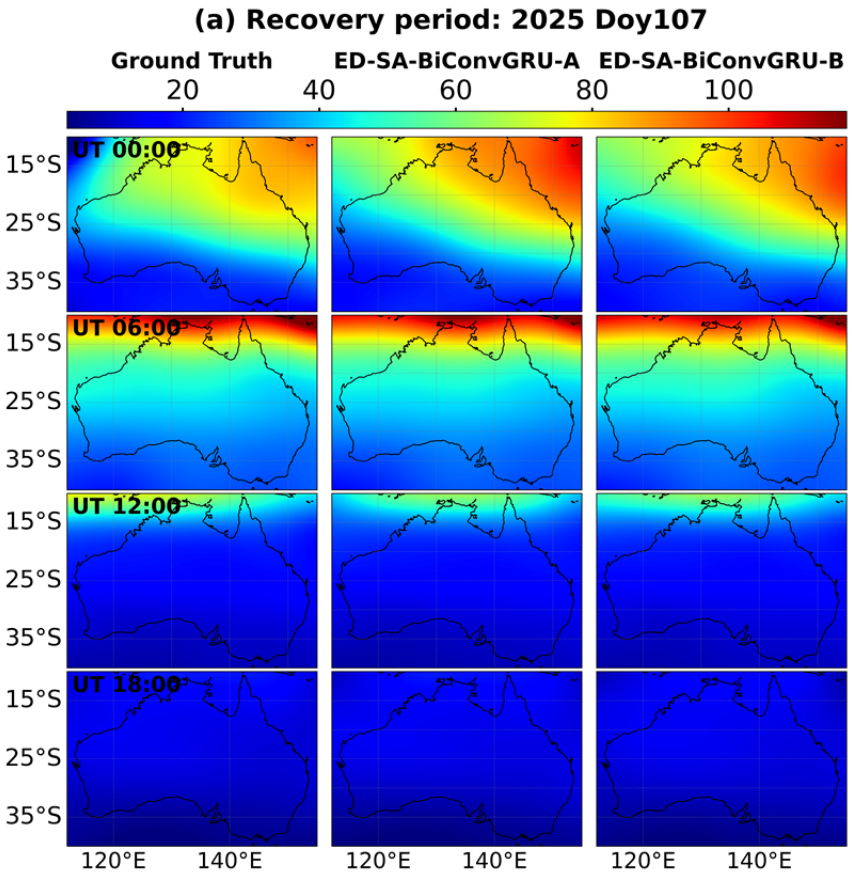


Fig. 4. Prediction residual of different combinations (TECu) during the main phase of the 2025 geomagnetic storm (DOY 105 and DOY 106).


(a) Recovery period: 2025 Doy107
Ground Truth
ED-SA-BiConvGRU-A
ED-SA-BiConvGRU-B
20
40
60
80
100
UT 00:00
UT 06:00
UT 12:00
UT 18:00
15°S
25°S
35°S
120°E
140°E

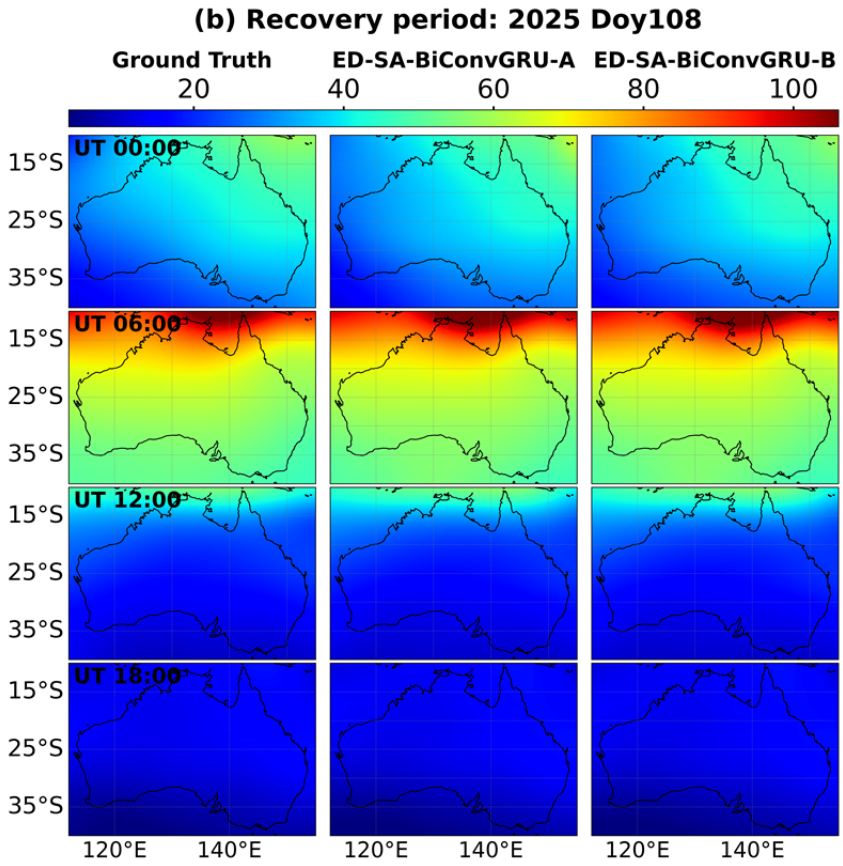


Fig. 5. Comparison of spatiotemporal prediction results (TECu) for different combinations during the recovery phase of the 2025 geomagnetic storm (DOY107 and DOY108).

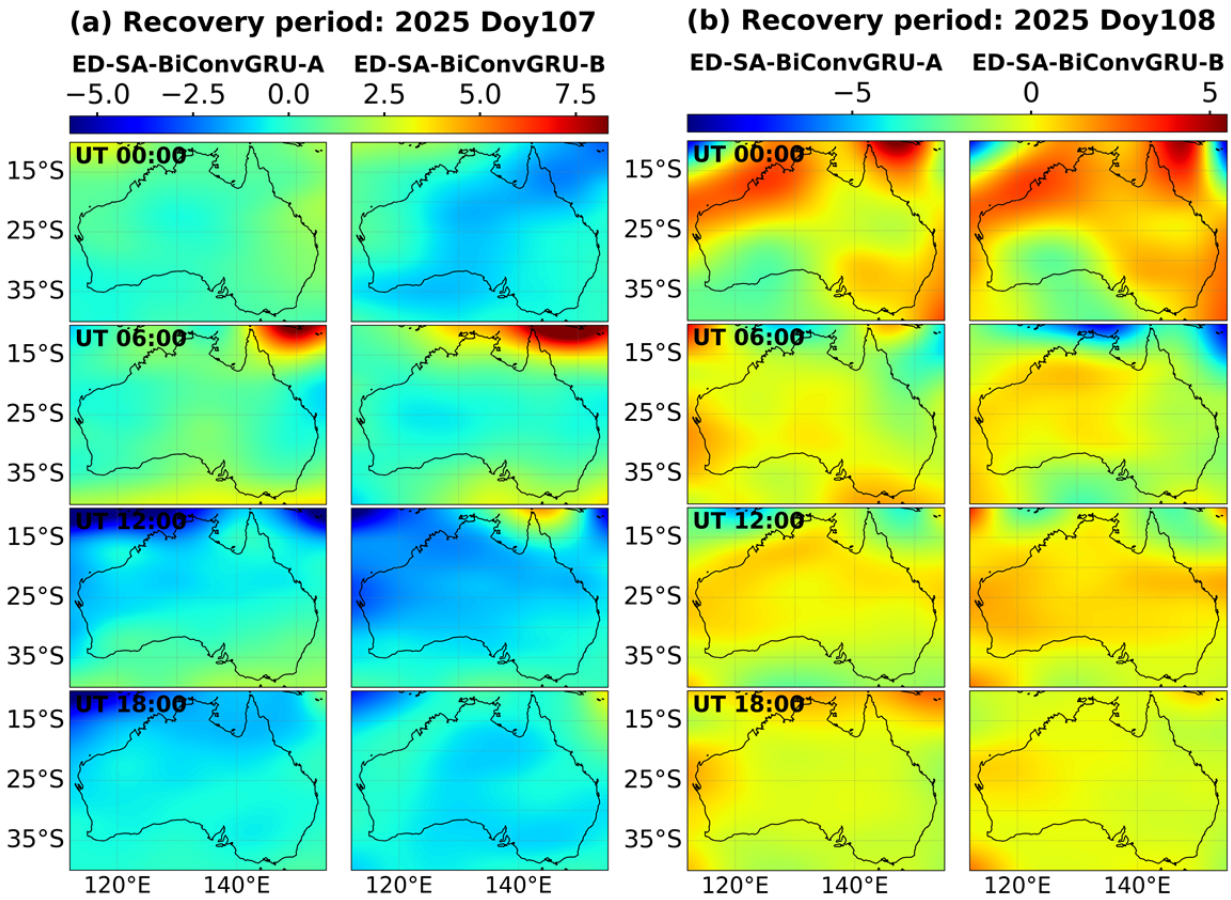


Fig. 6. Prediction residual of different combinations (TECu) during the recovery phase of the 2025 geomagnetic storm (DOY 107 and DOY 108).

COPYRIGHTED MATERIAL

The authors declare that no copyrighted material from third parties is used in this manuscript. All figures and tables are original or produced from open data.